Lead-halide templated crystallization of large-area methylamine-free perovskite films for efficient photovoltaic modules

Tongle Bu[1,2,3], Jing Li[1], Hengyi Li[1], Congcong Tian[1], Jie Su[4], Guoqing Tong[3], Luis K. Ono[3], Chao Wang[1], Zhipeng Lin[1], Nianyao Chai[1], Xiao-Li Zhang[5], Jingjing Chang[4], Jianfeng Lu[1,6], Jie Zhong[1,2], Wenchao Huang[1], Yabing Qi[3], Yi-Bing Cheng[2] and Fuzhi Huang[1,2]

[1]*State Key Laboratory of Advanced Technology for Materials Synthesis and Processing, Wuhan University of Technology, Wuhan 430070, PR China*

[2]*Xianhu Laboratory of the Advanced Energy Science and Technology Guangdong Laboratory, Foshan 528216, PR China*

[3]*Energy Materials and Surface Sciences Unit (EMSSU), Okinawa Institute of Science and Technology Graduate University (OIST), Okinawa 904-0495, Japan*

[4]*Xidian University, School of Microelectronics, State Key Discipline Lab of Wide Band Gap Semiconductor Technology, Shaanxi Joint Key Lab of Graphene, Advanced Interdisciplinary Research Center for Flexible Electronics, Xian 710071, PR China*

[5]*School of Materials Science and Engineering, Zhengzhou University, Zhengzhou 450001, PR China*

[6]*State Key Laboratory of Silicate Materials for Architectures, Wuhan University of Technology, Wuhan 430070, PR China*

Abstract

Upscaling efficient and stable perovskite light absorption layers is one of the most challenging issues in developing the next generation of photovoltaics for commercialization. Herein, we demonstrate a lead halide templated crystallization strategy for deposition of large-area compact and stable methylammonium (MA)-free perovskite films towards printable high-performance solar modules. High-quality large-area formamidinium (FA)-cesium (Cs) lead-triiodide perovskite films are achieved via controlled crystal growth of lead-halide•N-methyl-2-pyrrolidone (NMP) adduct. The adduct can react in situ with embedded FAI/CsI to directly form α-phase

perovskites to sidestep the phase transformation from δ-phase. The quality of the obtained perovskite films is further improved by incorporating a novel additive, potassium hexafluorophosphate (KPF_6). Incorporation of KPF_6 not only eliminates hysteresis but also enhances thermal stability by passivating interfacial defects. The modified devices feature a hysteresis-free high efficiency of over 23% with an excellent long-term thermal stability (@85℃) without encapsulation in ambient air (~80% efficiency retention after 500 hours). The slot-die printed mini-modules achieve champion efficiencies of 20.42% (certified efficiency 19.3%) and 19.54% with the active area of 17.1 cm^2 and 65.0 cm^2, respectively.

Hybrid organic-inorganic metal halide perovskite solar cells (PSCs) have attracted intensive interest during the last decade with the power conversion efficiency (PCE) boosting over 25% (*1*). Such a development is attributed to the intrinsically superior photoelectric properties of the perovskite materials that possess tunable bandgap, high absorption coefficient, and long carrier diffusion lengths (*2-4*). In particular, the PSCs can be fabricated *via* a myriad of low-cost solution processes, which offers great promise for future commercialization. However, scalability and stability issues have impeded its industrialization.

The most important prerequisite for fabricating large-area PSCs is the deposition of high-quality perovskite thin films. The nucleation and crystal growth of the perovskite in solution are largely uncontrollable, often leading to a porous film that would greatly impair the devices' performance (*5, 6*). The larger the area is, the harder it will be to achieve a uniform crystalline film. Various efforts have been devoted to controlling the nucleation and crystal growth for scaling up perovskite films. Many strategies, including anti-solvent bathing (*7*), softcover coating (*8*), gas flow (*9*), vacuum (*10*) or thermal assisting (*11*), and additive engineering (*12*) have been successfully used to fabricate high-quality large-area perovskite films. For example, Hu *et al.* employed an air-blade to quickly remove the solvent of the $MAPbI_3$ perovskite wet film to promote the concentration and induce a higher nucleation rate, forming a dense perovskite film (*13*). Huang *et al*. reported a thermal assist blade-coated perovskite film with an efficiency of 14.6% on 57.2 cm^2 perovskite solar modules (PSMs) using a surfactant added $MAPbI_{3-x}Cl_x$ perovskite ink (*11*).

However, $MAPbI_3$ perovskites have shown poor stability at high temperatures or

under light illumination (*14, 15*). Instead, the MA-free perovskites such as $FAPbI_3$ or $(FACs)PbI_3$ show promising thermal stability due to their higher phase transformation temperatures (*16-18*). In addition, the narrower optical bandgap of $FAPbI_3$ with respect to that of $MAPbI_3$ can contribute to higher efficiencies (*19*). Recently, the FA-based PSCs without MA have attracted intensive attention, especially for large-area devices (*20*). Unfortunately, the nucleation and crystal growth of the FA-based perovskites are even harder to control. Alternatively, it might be feasible to control the nucleation of perovskite intermediates such as its solvent-coordinated complexes (*9, 21*). However, it is found that the nucleation rate of solvent-coordinated FA-based perovskite complexes is still not high enough. Actually, besides the one-step method, the two-step method is also widely used in fabricating small-area perovskite films. It is rather easy to achieve a dense PbI_2 film in the first step, but it is hard for the FAI deposited in the second step to diffuse into the bottom of the PbI_2 film to induce a complete reaction (*22*). In the perovskite precursor solution, if the FAI and PbI_2 species do not form perovskites or solvent-coordinated perovskite complexes, the nucleation will be dominated by PbI_2 and therefore it will be easier to form a dense film. As FAI is embedded during the formation of the PbI_2 film, it is easier to induce an *in situ* reaction between the PbI_2 and FAI by the subsequent thermal annealing, resulting in a dense perovskite film. Thus, the crystallization of the perovskite is templated by the PbI_2-derived crystals.

Herein, we report a lead halide templated crystallization strategy to prepare compact methylamine-free perovskite films for the fabrication of anti-solvent-free and ambient-air printed high-performance PSMs. The key point to obtain high-quality large-area FA-based perovskite films is to completely inhibit the formation of solvent-coordinated perovskite intermediate complex via the formation of a stable PbI_2•*N*-methylpyrrolidone (NMP) adduct, which can react *in situ* with embedded FAI/CsI species. In addition, by this means we can lower the formation energy of α-phase perovskite that is an unstable high-temperature phase, thus convert the α-phase FA-based perovskite film ($FA_{0.83}Cs_{0.17}PbI_3$) even at room temperature. The resulting perovskite films are further passivated by a novel KPF_6 salt, which contributes to high-performance hysteresis-free perovskite solar cells with an efficiency of 23.35% and dramatically enhanced thermal and light stability. Eventually, a slot-die printed high-quality large-area perovskite film is realized using this strategy. The corresponding solar mini-modules demonstrate efficiencies of 20.42% on 17.1 cm^2 and 19.54% on

65.0 cm^2, respectively.

Nucleation and crystal growth study

$FAPbI_3$ has the narrowest band-gap (~1.48 eV) among the Pb-based perovskites and much better thermal stability than MA-based perovskite. However, pure α-$FAPbI_3$ is unstable, so Cs is normally introduced to stabilize the phase (*23*). Here $FA_{0.83}Cs_{0.17}PbI_3$ perovskite is employed to study its nucleation and crystal growth kinetics. *N*,*N*-dimethylformamide (DMF) is a commonly used solvent for perovskite precursor ink due to its high solubility and volatility. It is found that during the natural drying process, only a few nuclei form at the beginning (fig. S1-i), then several flat needle-shaped crystals grow surrounding every nucleus. After drying completely, the SEM image (Fig. 1A-i) shows a rough film with dendrites, large pores, and some densely packed large grains lying underneath the dendrites, clearly indicating there are two types of structures. To trace the formation processes of such structures, *in situ* XRD is conducted to investigate phase change during the natural drying process. According to the DFT fitting (fig. S2) and comparing them with the *in situ* XRD patterns from different components with additives (fig. S3), it can be inferred from Fig. 1B-i and fig. S4A that at the beginning, solvent-coordinated perovskite intermediate phases of $Cs_2Pb_3I_8$•4DMF and $FA_2Pb_3I_8$•4DMF form and then transform to δ-(FACs)PbI_3. Finally, $FA_2Pb_3I_8$•4DMF and δ-(FACs)PbI_3 mainly present in the film. Although perovskites in the DMF form intermediate solvent-coordinated complexes, the nucleation rate is still too low in the natural drying process. To accelerate the nucleation rate, the precursor solution is spun at 3000 rpm to quickly remove the solvent. The morphology change is shown in Fig. 1C-i. There are some large area dense zones formed, with a few rods randomly distributed. So even with the assistance of solvent removal by spinning, the nucleation rate is not high enough, as there are still many large pores. This demonstrates it is hard to change the nucleation kinetics of FA-based perovskites through the approach of forming intermediate solvent-coordinated complexes. The XRD patterns (Fig. 1D-i) show the presence of major δ-(FACs)PbI_3 in the final film.

In our initial study, we found that NMP can form a strong PbI_2•NMP adduct, (fig. S3, fig. S4B). As proposed, if PbI_2•NMP can remain in the perovskite precursor solution, the nucleation will be dominated by the PbI_2•NMP adduct. After the formation of the film, the FAI/CsI species are also homogenously distributed in the film. It is very easy

to induce the reaction of PbI_2 and FAI/CsI in the film by thermal annealing. Thus, the film morphology will be well controlled. Then the NMP with the molar ratio of 1:1 to PbI_2 is added into the $FA_{0.83}Cs_{0.17}PbI_3$/DMF solution. Similar studies are carried out and we find that there are two types of the nucleus (fig. S1-ii). The nuclei inducing the growth of needle-shaped crystals have no obvious change, but the length of the needle becomes a little shorter, indicating that the growth of the solvent-coordinated perovskite complexes is suppressed. More importantly, a large number of the second type of nuclei form, growing into spherical particles. Through the *in situ* XRD (Fig. 1B-ii), it is found that the initial strong peaks of $FA_2Pb_3I_8$•4DMF become weaker and the later appeared PbI_2•NMP peaks become stronger, leaving the final film consisting of $FA_2Pb_3I_8$•4DMF and PbI_2•NMP. The SEM image (Fig. 1A-ii) also shows in the rough film there are two types of structure, densely packed particles in the layered structure and some dendrite structure originated from the $FA_2Pb_3I_8$•4DMF. When the film is prepared by spin-coating the precursor solution at 3000 rpm, the film becomes smoother and denser, in a light brown color (fig. S5), but still having some small pores and several needles (Fig. 1C-ii). XRD patterns (Fig. 1D-ii) show the presence of almost pure PbI_2•NMP phase. Interestingly, we also find that minor α-(FACs)PbI_3 emerges in the film. When we increase the spinning speed to 5000 rpm, the peak intensity of α-phase becomes stronger (fig. S6). It is completely different from that of the film derived from the pure DMF solution. When the film is annealed at 70 ℃, α-(FACs)PbI_3 phase appears obviously (Fig. 1D-ii), and the film becomes a black color (fig. S5). With further increase in annealing temperature to 150 ℃, the peak of α-phase becomes even stronger. For the DMF-derived film, when annealed at 70 ℃, the peak of δ-(FACs)PbI_3 phase becomes stronger (Fig. 1D-i) and the film still remains a yellow color (fig. S5). However, when further annealed at 150 ℃, the δ-phase is completely transformed into α-phase (Fig. 1D-i) and becomes a black color (fig. S5). According to the DFT calculation (Fig. 1F), as α-$FAPbI_3$ is a high-temperature phase, the conversion energy is high if it is from the δ-$FAPbI_3$ which is transformed from the DMF coordinated complexes rapidly. However, when PbI_2•NMP reacts with FAI to form perovskite, the α-$FAPbI_3$ formation energy is dramatically decreased. This is why the addition of NMP can induce α-phase perovskite at room temperature with the incorporation of Cs. The study of pure $FAPbI_3$ films growing from 2-methoxyethanol (2-Me), an uncoordinated solvent, with/without corresponding coordination solvent additives, further confirms the above findings as shown in fig. S7. In short, the presence of the intermediate phases (the perovskite-DMF

complexes) will result in porous δ-phase perovskite films, while the existence of PbI_2-NMP will directly produce dense α-phase perovskite films (fig. S4E). Therefore, an improved quality of perovskite film can be obtained by inhibiting the formation of the perovskite-DMF complexes.

Therefore, it is more preferable if α-(FACs)PbI_3 is directly formed from the solution without second phase transformation, which would suppress the formation of defects and traps during the δ- to α-phase transition. From the above results, we can conclude that in the (FACs)PbI_3 perovskite DMF solution, it is likely to form solvent-coordinated perovskite intermediate phases of $Cs_2Pb_3I_8$•4DMF and $FA_2Pb_3I_8$•4DMF that later convert to δ-(FACs)PbI_3 and thus result in poor morphology, as depicted in Fig. 1E. When NMP is added, the intermediate phases of $Cs_2Pb_3I_8$•4DMF and $FA_2Pb_3I_8$•4DMF are restrained by the competition of PbI_2•NMP, resulting in the formation of α-(FACs)PbI_3. To further improve the film quality, the intermediate phase of $FA_2Pb_3I_8$•4DMF should be completely inhibited. By the further introduction of excess $PbCl_2$ to the precursor solution, we find that the growth of the $FA_2Pb_3I_8$•4DMF nuclei is further suppressed by the formation of an additional PbX_2•0.5NMP•0.5DMF adduct as shown in fig. S1-iii, and the film becomes much denser (Fig. 1A-iii), more transparent, and in a brown color (fig. S5), indicating much faster nucleation of lead halide-NMP adducts and effective suppression of δ-phase formation. Further evidence can be found from the *in situ* XRD patterns (Fig. 1B-iii) showing the presence of a much lower peak of $FA_2Pb_3I_8$•4DMF and the SEM image of the spin-coated film showing negligible pores (Fig. 1C-iii). The related XRD patterns (Fig. 1D-iii) of the spin-coated film show the presence of PbI_2•NMP and PbX_2•NMP/DMF complexes without $FA_2Pb_3I_8$•4DMF. The XRD patterns (fig. S6) and SEM images (fig. S8) indicate a relatively low volatilization rate of the precursor solution during the deposition (spin rate > 3000 rpm) is sufficient to achieve dense perovskite films even without anti-solvent process. The annealing even at 70 ℃ could induce a stronger peak of α-$FAPbI_3$ phase. The additional peak belonging to PbI_2 at 150 ℃ is due to the added excess PbX_2. The excess PbI_2 is generally beneficial to the device by the passivation (*24*).

Photovoltaic performance

To study the corresponding films' device performance, we employed a normal structure of FTO/SnO_2/perovskite/spiro-OMeTAD/Au. To be feasible for industry, we adopt a

two-step annealing process for perovskites, namely a 70 °C annealing in the glovebox to dry the films, followed by another 150 °C annealing in air to promote the crystal growth with the assistance of humidity. The champion *J-V* curves of PSCs are shown in fig. S9. The devices made from pure DMF-derived perovskite films exhibit a poor PCE of 7.64%, while the NMP engineered perovskite devices show a much higher efficiency over 20%. We further modulated the addition of $PbCl_2$ and obtained mirror-like black films (fig. S5). The efficiencies are improved significantly with the increasing amount of $PbCl_2$ no more than 10%, while the hysteresis is keeping decreasing. A champion efficiency of 21.92% is achieved by the addition of 10% $PbCl_2$ (fig. S9). After further characterization of the crystal properties by XRD, UV-Vis and SEM for the different amounts of $PbCl_2$-containing perovskite films (fig. S10), It is found that the intrinsic reasons for the improved performance by introducing $PbCl_2$ are the suppression of δ-phase formation, improvement of coverage with increased grain size, and the *in situ* formation of PbI_2 at the grain boundary as a passivator (Fig. S10) due to the substitution of I^- or I^- vacancies by Cl^- to form a $FA_{0.83}Cs_{0.17}PbI_{3-x}Cl_x$ perovskite (*25, 26*).

To further improve the performance, we introduced a post-treatment of bromide based large cation salt (isobutylamine bromide, iBABr) on the as-fabricated $FA_{0.83}Cs_{0.17}PbI_{3-x}Cl_x$ (labeled as 3D perovskite) surface to form a 3D/2D structured perovskite layer according to previous reports (*27*, *28*) (fig. S11), which would contribute to the stability improvement and V_{oc}-loss reduction for the solar cells. The corresponding device structure is shown in Fig. 2A. An improved efficiency of 23.02% under reverse scan (RS) for the 3D/2D perovskite-based solar cells is achieved, with a V_{oc} of 1.166 V, a short-circuit current density (J_{sc}) of 23.97 mA/cm^2 and a fill factor (FF) of 0.824. A lower efficiency of 20.71% is achieved under forward scan (FS), with a V_{oc} of 1.142 V, J_{sc} of 24.01 mA/cm^2 and a fill factor (FF) of 0.755, respectively (Fig. 2B). An obvious hysteresis with a hysteresis index (HI) of 0.10 is still present.

Stability improvement

Hysteresis is related to the stability that is one of the major obstacles to the commercialization of PSCs (*29*). To eliminate the hysteresis and further improve the photovoltaic performance and stability, we employed a novel potassium-based salt, KPF_6, as an additive to the perovskite precursor solution. XRD, UV-Vis and SEM

characterizations (fig. S12) confirm the incorporation of KPF_6 to perovskites. The corresponding photovoltaic characteristics are shown in fig. S13. With the addition of KPF_6, the hysteresis is keeping decrease and the hysteresis index (HI) reaching to 0.00 at the concentration of 5% additives. To accurately evaluate the real PCE, steady-state power output (SPO) measurement is conducted. It can be found with the lower HI, the PCE from SPO becomes closer to the PCE from *J-V* scans. When the concentration is above 0.5%, the hysteresis is actually almost negligible. A champion efficiency is obtained with the addition of 1.5 mol% KPF_6 salts (labeled as 3D/2D-KPF_6), showing a higher V_{oc} of 1.178 V, a J_{sc} of 24.03 mA·cm^{-2}, a FF of 0.825 and a PCE of 23.35% under RS, and a V_{oc} of 1.175V, a J_{sc} of 24.06 mA·cm^{-2}, a fill factor (FF) of 0.818 and a PCE of 23.13% under FS. The average PCE of 23.24% is very close to the PCE from SPO of 23.2%, much higher than the control device (21.9%) (fig. S14A). It is not surprising to see when further adding of KPF_6 decreases the PCE although having no hysteresis, as too much KPF_6 will affect the nucleation behavior and lead to poorer film morphology (fig. S12C). The corresponding external quantum efficiency (EQE) spectra show an integrated J_{sc} of 23.70 mA·cm^{-2} and 23.78 mA·cm^{-2} for devices with and without KPF_6, respectively (fig. S14B), which match well with the measured J_{sc}. In addition, the PSCs in the size of 1.0 cm^2 also exhibit significant improvements of PCEs, increasing from 21.92% (RS) and 19.31% (FS) to 22.53% (RS) and 22.27% (FS) with the addition of KPF_6 (Fig. 2C, table S2). The distribution of *J-V* parameters for both small area and 1.0 cm^2 sized cells processed with or without KPF_6 additives are shown in fig. S15. Ultraviolet photoemission spectroscopy (UPS) and UV-Vis absorption spectroscopy (fig. S16) characterizations reveal the lifted CB minimum from -4.14 eV for 3D perovskite to -4.10 eV for 3D/2D perovskite, and further to -3.94 eV for 3D/2D-KPF_6 perovskite, which contributes to the enhanced V_{oc} of the modified devices.

We further used the space-charge-limited current (SCLC) measurements to characterize the trap density of these different films (*30-32*). The calculated defect density decreases from 6.17×10^{15} cm^{-3} to 4.97×10^{15} cm^{-3}, indicating the reduced defects of the perovskite film with the addition of KPF_6 (Fig. 2D). The time-resolved confocal PL microscopy measurement was also performed to characterize the charge carrier properties of these perovskite films in micro-size (10 μm × 10 μm) (Fig. 2E to F). The blue region with a short PL lifetime for the pristine 3D/2D perovskite transits to a green region with a much longer PL lifetime after the addition of KPF_6. It indicates a reduced trap-induced or non-radiative recombination by the defect passivation due to the

addition of KPF_6, thus resulting in a small V_{oc} loss of ~0.37 eV (fig. S17). This passivation strategy would be beneficial to stability.

Fig. 3A shows the thermal stability of widely researched CsFAMA triple-cation-based perovskite ($(Cs_{0.05}(FA_{0.85}MA_{0.15})_{0.95})Pb(I_{0.85}Br_{0.15})_3$) and our MA-free perovskite ($FA_{0.83}Cs_{0.17}PbI_3$) based solar cells measured at 85 ℃ in ambient air (15 ± 5% relative humidity). The efficiency of CsFAMA devices quickly decreases to 2.9 ± 3.1% within 360 hours. Obvious holes are observed from the cross-sectional SEM image due to the degradation of the CsFAMA device after aging at 85 ℃ (fig. S18). Although the MA-free 3D/2D devices exhibit a significant improvement and remain the black appearance, the devices still show a salient decrease after aging at 85 ℃ for 500 hours, remaining less than 50% of the initial efficiency. However, this degradation can be significantly suppressed with the addition of KPF_6. The 3D/2D-KPF_6 devices exhibit ~80% of the initial efficiency after aging at 85 ℃ for 500 hours. The *J-V* curves of different devices under the thermal stability measurements are plotted in fig. S19. It can be found that there is a negligible change of FF in the device processed with KPF_6, indicating the undamaged interfaces of devices.

This significant improvement in stability can be ascribed to the PF_6^- induced complex in perovskite films. The complex stays on the surface, passivating the grain boundaries, as seen from the SEM images (fig. S12C). In addition, to unravel the distribution of PF_6^- complex across the perovskite layer, we conducted time-of-flight secondary-ion mass spectrometry (TOF-SIMS) for 1.5 mol% KPF_6 contained $FA_{0.83}Cs_{0.17}PbI_{3-x}Cl_x$ perovskite film (Fig. 3B). A block-by-block distribution of the agglomerated PF_6^- ions is shown in the three-dimensional visualization images. The corresponding depth profiles of TOF-SIMS and X-ray photoelectron spectroscopy (XPS) also show detected signals of K and F elements throughout the perovskite films (fig. S20 A-C). In addition, FTIR spectra show the N-H and P-F corresponding peaks shift to lower wavenumbers with the increasing amount of KPF_6 additives, revealing the presence of the hydrogen bonding between perovskite and PF_6^- (fig. S20 D-F). Thus, it would greatly affect both the perovskite grain boundary and interfacial properties of devices, contributing to better performance by passivating the surface defects.

The corresponding cross-sectional SEM images of the thermal aged devices with or without KPF_6 additives are shown in Fig. 3C to D. It is found that there is no obvious change of the perovskite/spiro-OMeTAD interface with the KPF_6 additive, while the

interface becomes intersected if without the KPF_6 additive. We further employed TOF-SIMS characterization to probe the thermal aged devices and fresh devices (Fig. 3E to F, fig. S21). In the device without KPF_6, Cs, Pb and I ions are shifted toward the spiro-OMeTAD layer. The Co ions that are a dopant in spiro-OMeTAD diffuse into the perovskite layer after thermal aging (Fig. 3E), matching well with the above SEM finding. With KPF_6, the diffusion of ions is significantly suppressed (Fig. 3F).

We also measured the light illumination stability of the devices. The solar cells were continuously measured for 5 times under one sun AM 1.5G. A rapid degradation of V_{oc} and FF for the 1.0 cm^2 3D/2D perovskite solar cell is observed, while the KPF_6 modified device exhibits negligible degradation (fig. S22). The long-term light illumination stability was also characterized as shown in fig. S23A. The champion device with KPF_6 additives exhibits a better photo-stability than the pristine device, remaining 82% of its initial efficiency after 500 hours under continuous AM 1.5G solar illumination without a UV-filter, at an open-circuit condition that is said harsher than the operation condition (*33*). A more stable statistic PCE evolution of the devices with KPF_6 additive compared with the pristine devices is seen in fig. S23B. Therefore, the KPF_6 additive plays an important role in improving the stability of perovskite devices as well.

Ambient-air printed photovoltaic modules

As the dense perovskite films can be easily prepared by spin-coating of the developed ink at a relatively low speed, similarly a moderate dry-air gas can also promote nucleation (fig. S24A). Thus, a gas-assist slot-die printing technology towards the continuous deposition of large-area perovskite films is developed here, as demonstrated in Fig. 4A. With a low pressure of ~0.3 MPa dry air blowing, the printed wet perovskite film quickly changes to a brown color with a mirror-like surface, as shown in Movie S1. The inset in Fig. 4A presents the photograph of the printed large-area 20 cm × 20 cm perovskite film. A pinhole-free high-quality perovskite layer with clear grain boundaries is shown in the SEM image (fig. S24B).

The 5 cm × 5 cm PSMs are then fabricated, and the *J-V* curves are shown in Fig. 4B. The inset shows the schematic diagram of a 6 sub-cell series-connected 5 cm × 5 cm module, and fig. S25 shows its photo. The slot-die printed PSM shows comparable

performance to the spin-coating counterpart (Fig. 4B) with efficiencies over 20.4% (table S1). Certified efficiencies of 19.3% and 18.9% with a mask area of 17.1 cm^2 are achieved respectively for the slot-die printed and spin-coated PSMs (fig. S26-27). The hysteresis-suppression effect of KPF_6 is also proven in large solar modules, exhibiting much stable efficiency (fig. S28A to B). We also achieved a champion FF of 0.806 for a 4 cm × 4 cm solar module (mask area = 10.0 cm^2) (fig. S28C), which is the highest record among the reported perovskite solar modules. Furthermore, it also shows excellent performance under weak light illumination and continuous multiple testing (fig. S28D). It indicates the super uniformity of large-area perovskite films achieved from this lead-halide templated crystallization strategy, contributes to high-performance solar modules.

We further scaled up the perovskite films to print a 10 cm × 10 cm solar module with a series connection of 14 subcells, and demonstrated a hysteresis-free solar module with high efficiency of 19.54% under RS and 19.22% under FS with a mask area of 65.0 cm^2 (Fig. 4C). The module efficiencies from different upscaling methods with different active areas during the past years are summarized in Fig. 4D. The anti-solvent-free modulated high-quality perovskite films in this work exhibit the highest efficiencies among all the reported works, indicating the high processability for achieving large-area high-quality perovskite films.

REFERENCES AND NOTES

1. NREL, **https://www.nrel.gov/pv/cell-efficiency.html**, (2021).
2. S. D. Stranks *et al.*, *Science* **342**, 341-344 (2013).
3. D. Shi *et al.*, *Science* **347**, 519-522 (2015).
4. Q. Dong *et al.*, *Science* **347**, 967-970 (2015).
5. F. Huang *et al.*, *Nano Energy* **10**, 10-18 (2014).
6. M. Xiao *et al.*, *Angew. Chem. Int. Ed.* **53**, 9898-9903 (2014).
7. Y. Y. Kim *et al.*, *Nat. Commun.* **11**, 5146 (2020).
8. H. Chen *et al.*, *Nature* **550**, 92-95 (2017).
9. Y. Deng *et al.*, *Sci. Adv.* **5**, eaax7537 (2019).
10. Z. Xu *et al.*, *J. Mater. Chem. A* **7**, 26849-26857 (2019).
11. Y. Deng *et al.*, *Nat. Energy* **3**, 560-566 (2018).
12. C. Li *et al.*, *J. Am. Chem. Soc.* **141**, 6345-6351 (2019).
13. J. Ding *et al.*, *Joule* **3**, 402-416 (2019).
14. B. Conings *et al.*, *Adv. Energy Mater.* **5**, 1500477 (2015).
15. E. J. Juarez-Perez *et al.*, *J. Mater. Chem. A* **6**, 9604-9612 (2018).
16. S.-H. Turren-Cruz *et al.*, *Science* **362**, 449-453 (2018).

17. Yen-Hung Lin *et al.*, *Science* **369**, 96-102 (2020).
18. X. X. Gao *et al.*, *Adv. Mater.* **32**, e1905502 (2020).
19. Mingyu Jeong *et al.*, *Science* **369**, 1615-1620 (2020).
20. M. Du *et al.*, *Adv. Mater.* **32**, e2004979 (2020).
21. N. Ahn *et al.*, *J. Am. Chem. Soc.* **137**, 8696-8699 (2015).
22. F. Guo *et al.*, *Adv. Funct. Mater.* **29**, 1900964 (2019).
23. M. Saliba *et al.*, *Energy Environ. Sci.* **9**, 1989-1997 (2016).
24. Q. Jiang *et al.*, *Nat. Energy* **2**, 16177 (2016).
25. A. Ren *et al.*, *Joule* **4**, 1263-1277 (2020).
26. M. I. Saidaminov *et al.*, *Nat. Energy* **3**, 648-654 (2018).
27. Yuhang Liu *et al.*, *Angew. Chem. Int. Ed.* **59**, 15688 -15694 (2020).
28. D. Luo *et al.*, *Science* **360**, 1442-1446 (2018).
29. P. Liu *et al.*, *Adv. Energy Mater.* **9**, 1803017 (2019).
30. Z. Liu *et al.*, *Nat. Commun.* **9**, 3880 (2018).
31. E. A. Duijnstee *et al.*, *ACS Energy Lett.* **5**, 376-384 (2020).
32. J. Chen *et al.*, *Adv. Mater.* **30**, e1801948 (2018).
33. K. Domanski *et al.*, *Nat. Energy* **3**, 61-67 (2018).
34. T. Bu *et al.*, *Solar RRL* **4**, 1900263 (2019).
35. J. Li *et al.*, *Joule* **4**, 1035-1053 (2020).
36. X. Dai *et al.*, *Adv. Energy Mater.* **10**, 1903108 (2019).

ACKNOWLEDGMENTS

Funding: This work is financially supported by the National Key Research and Development Plan (SQ2019YFE010779, SQ2017YFE0131900), the National Natural Science Foundation of China (21875178, 91963209), and Foshan Xianhu Laboratory of the Advanced Energy Science and Technology Guangdong Laboratory (XHD2020-001, XHT2020-005). The Analytical and Testing Centre of Wuhan University of Technology and Hubei Key Laboratory of Low Dimensional Optoelectronic Material and Devices, Hubei University of Arts and Science are acknowledged for the XRD and SEM characterizations. G.T., L.K.O., and Y.B.Q. acknowledge the funding support from the Energy Materials and Surface Sciences Unit of the Okinawa Institute of Science and Technology Graduate University. **Author contributions:** F.H. and T.B. conceived the ideas and designed the experiments. Y.B.C. provided helpful advices to the work. T.B. conducted the corresponding device and module fabrication and basic characterization. J.L., H.L. and C.T helped with the module fabrication, encapsulation. J.L. and C.W. helped with the efficiency certification of modules. T.B. and J.S. conducted the DFT calculation. G.T. and L.K.O. helped with the XPS, UPS characterization and analyses. Z.L. and N.C. helped with the stability test. J.C., J.L.,

J.Z., X.L.Z, W.H., Y.B.Q., Y.B.C. provided valuable suggestions for the manuscript. F.H. and T.B. participated in all the data analysis. F.H. and T.B. wrote the paper, and all authors revised the paper. **Competing interests:** None declared. **Data and materials availability:** All data needed to evaluate the conclusions in the paper are present in the paper or the supplementary materials.

SUPPLEMENTARY MATERIALS

Supplementary Materials

Materials and Methods

Table S1 – S3

Fig S1 – S28

References (37 – 43)

Movie S1

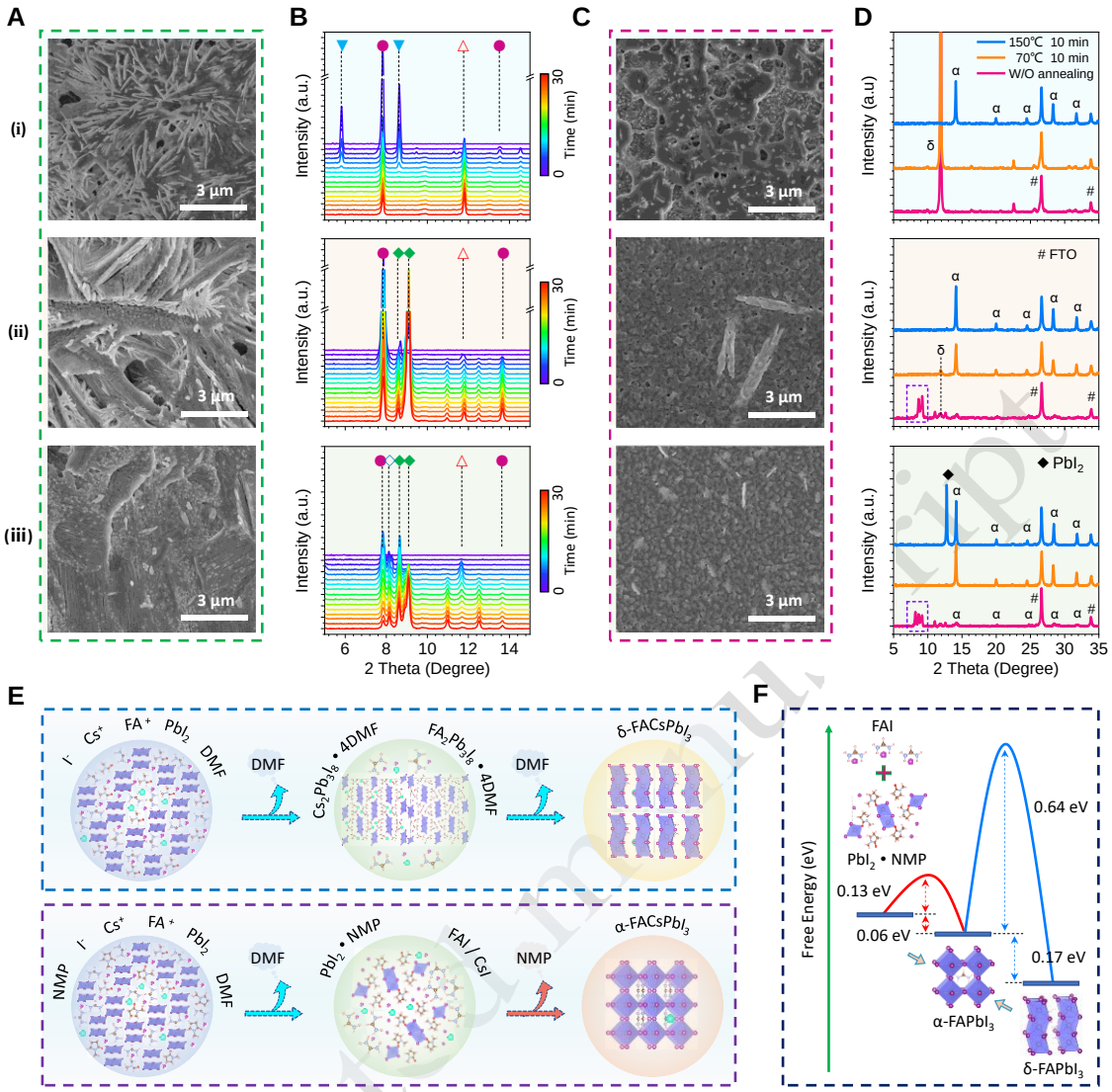

Fig. 1. Nucleation and crystallization of MA-free perovskites. (**A**) SEM and (**B**) *in situ* XRD patterns of 10 μL perovskite precursor ink (1.1 M) with/without different additives drying on the 1.5 cm × 1.5 cm FTO/glass substrates: (i) $FA_{0.83}Cs_{0.17}PbI_3$/DMF, (ii) $FA_{0.83}Cs_{0.17}PbI_3$-NMP/DMF, (iii) $FA_{0.83}Cs_{0.17}PbI_3$-NMP-10%$PbCl_2$/DMF. (**C**) SEM images of the corresponding perovskite ink spun onto FTO/glass substrates @ 3000 rpm. (**D**) The corresponding XRD patterns of spin-coated (@3000 rpm) perovskite films annealed at different temperatures for 10 min. (**E**) Schematic diagram of crystal growth with/without NMP. (**F**) Free energy calculation for the formation of $FAPbI_3$ perovskites with/without NMP.

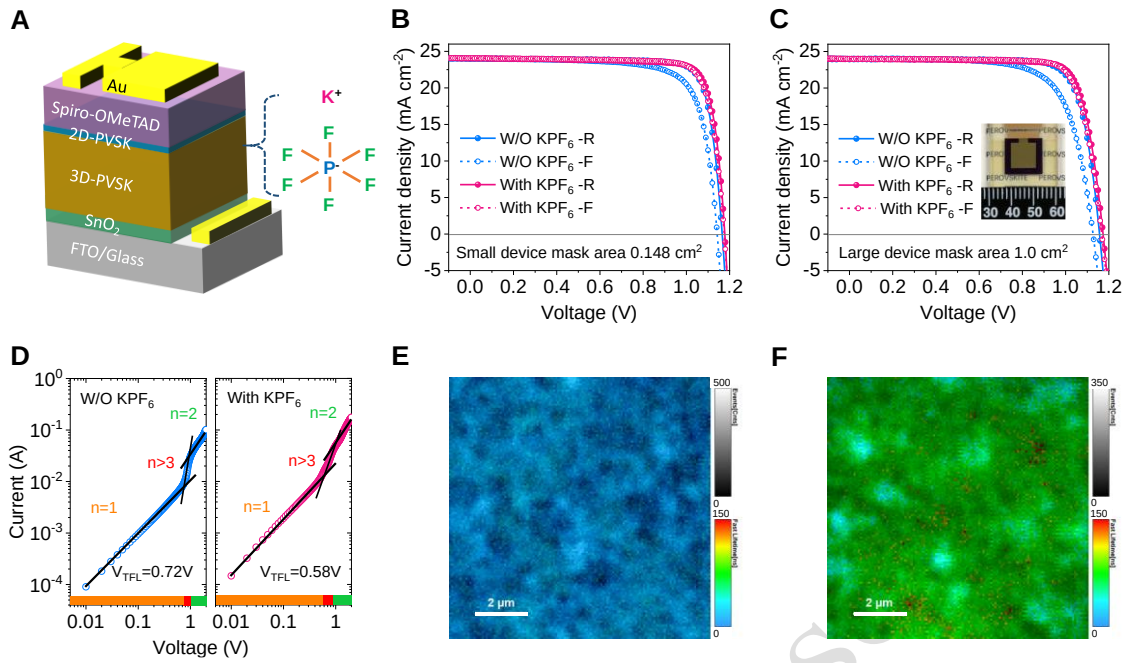

Fig. 2. Photovoltaic performance of anti-solvent-free coated PSCs with KPF_6 passivation. (**A**) Schematic of the PSC with the structure FTO/SnO_2/3D-perovskite/2D-perovskite/spiro-OMeTAD/Au. Champion *J-V* curves of 3D/2D perovskite-based devices with/without KPF_6 additive tested using a metal mask with an aperture area of (**B**) 0.148 cm^2 and (**C**) 1.0 cm^2. (**D**) *J*−*V* characteristics of the 3D/2D perovskite films with/without KPF_6 additive derived from the SCLC measurements with a structure of ITO/perovskite/Au. Time-resolved confocal PL lifetime maps of (**E**) 3D/2D and (**F**) 3D/2D-KPF_6 perovskite films, respectively.

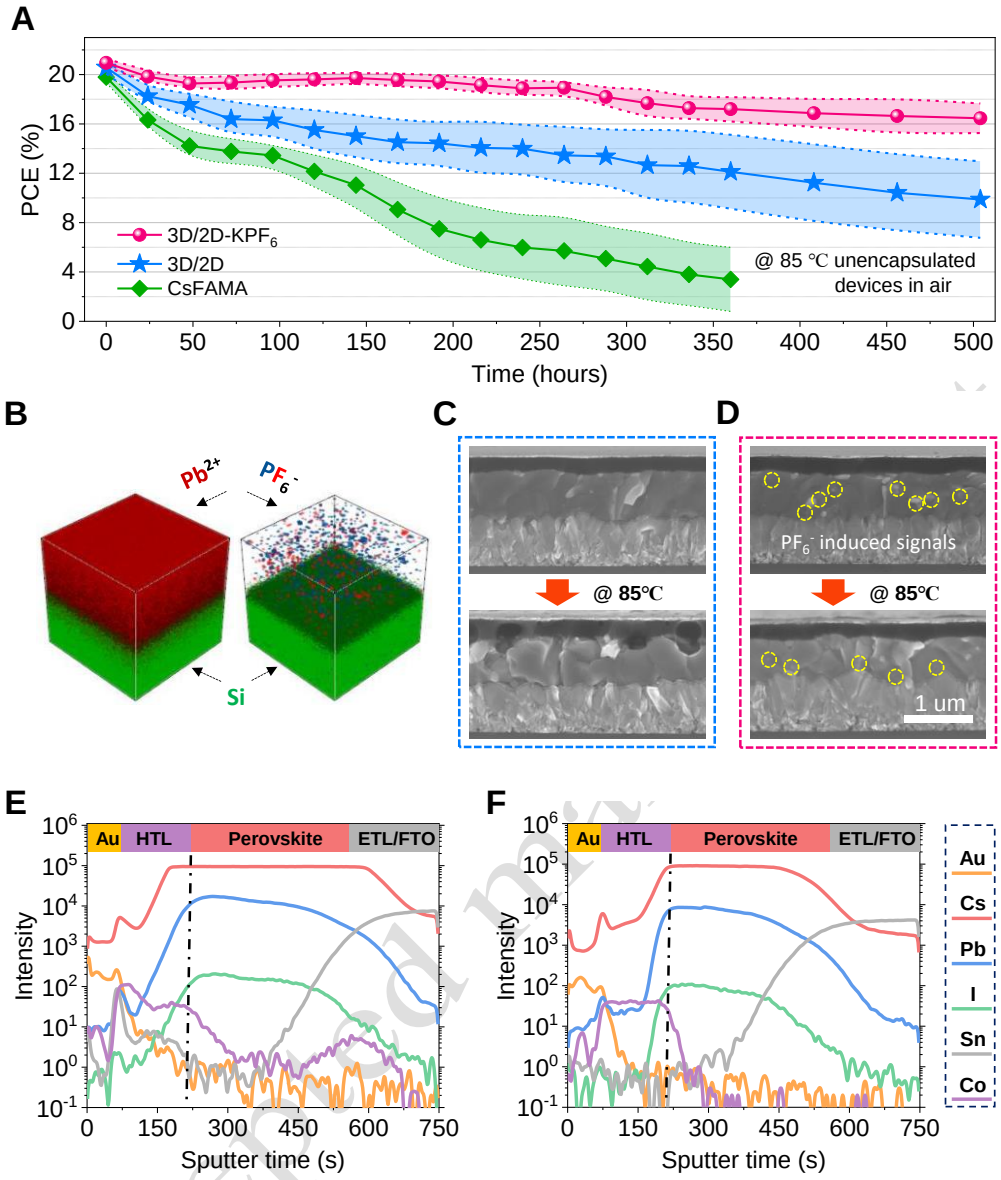

Fig. 3. Thermal stability characterization. (**A**) Average PCE evolution of the unencapsulated devices measured over a 500-hour stability test at 85 °C in ambient air (eight cells for each test condition, relative humidity ~15±5%). (**B**) Time-of-flight secondary ion mass spectrometry (TOF-SIMS) of Pb, P and F ions in the $FA_{0.83}Cs_{0.17}PbI_3Cl_x$ perovskite film with KPF_6 additive on a Si substrate (measurement area 80 μm × 80 μm). Cross-sectional SEM images of different devices, (**C**) Fresh 3D/2D device before/after 360 hours 85 ℃ aging; (**D**) Fresh 3D/2D-KPF_6 device before/after 360 hours 85 ℃ aging. TOF-SIMS spectra of (**E**) 3D/2D and (**F**) 3D/2D-KPF_6 devices after 360 hours 85 ℃ aging.

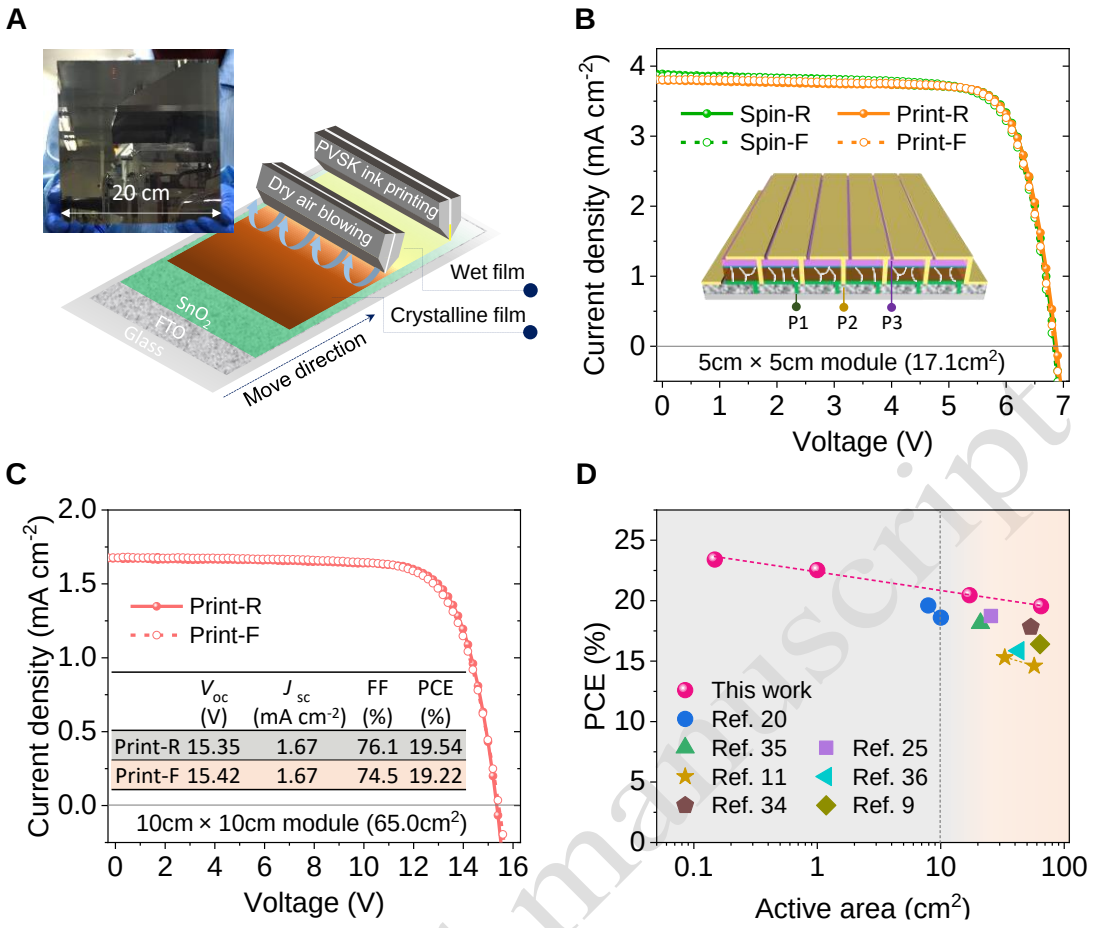

Fig. 4. Photovoltaic performance characterization of large-area modules. (**A**) Schematic illustration for the slot-die printing of perovskite films with low-pressure dry air blowing. Inset shows a photo of a printed 20 cm × 20 cm perovskite film. (**B**) Champion *J-V* curves of the 5 cm × 5 cm mini-modules based on the anti-solvent free spin-coating method and slot-die printing method. The inset shows the schematic diagram of a 6 sub-cells series-connected module. (**C**) Champion *J-V* curves of the 10 cm × 10 cm mini-module using the slot-die printing method fabricated large-scale perovskite film. (**D**) Champion efficiencies of PSCs as a function of the active area from this work and recent representative reports (*9, 11, 20, 25, 34-36*).